Surface Science 640 (2015) 65–72

Contents lists available at ScienceDirect

Surface Science

journal homepage: www.elsevier.com/locate/susc

Correlating Structure and Function of Metal Nanoparticles for Catalysis

Liang Zhang [a,c], Rachel M. Anderson [a,b], Richard M. Crooks [a,b], Graeme Henkelman [a,b,c,*]

[a] Department of Chemistry, The University of Texas at Austin, Austin, TX 78712–0165, United States
[b] Texas Materials Institute, The University of Texas at Austin, Austin, TX 78712–0165, United States
[c] Institute for Computational Engineering and Sciences, The University of Texas at Austin, Austin, TX 78712–0165, United States

ARTICLE INFO

Available online 2 April 2015

Keywords:
Nanoparticle
Structure
Function
Alloy
Catalysts
Core-shell

ABSTRACT

This paper summarizes several studies correlating the structure and function of nanoparticle catalysts. Three types of alloy nanoparticles are considered, random alloy, core@shell and alloy-core@shell structures. In the first two cases, the focus is to build theoretical models to understand previous experimental results. In the latter case, calculations play a greater role in leading the development of nanoparticle catalysts. We demonstrate that iteration between theory and experiment can facilitate an understanding of nanoparticle catalysts and reduce the time and effort involved in the design of new catalysts.

1. Introduction

The science and technology of catalysis is particularly important at this time due to the energy and environmental challenges facing society. Research in the 1990s, showing surprising activity of Au nanoparticles, has largely motivated a search for new catalytic materials on the nanoscale with properties that are different from their bulk counterparts. [1] Another significant factor in the development of new catalysts has been the growth of computing power and improvements in theoretical methods to help understand experiments at the atomic scale and to provide guidelines for catalyst design. Experiments, demonstrating the high activity of nanoparticle catalysts, have inspired the development of theoretical methods for calculating reaction mechanisms and screening for new catalysts. Iterating between theory and experiment is a promising strategy for understanding nanoparticle catalysis and reducing the cost of the development cycle for new catalysts. This paper reviews some of our recent theoretical studies of multi-metallic nanoparticles catalysis, and shows how, with a close coupling to experiment, we are able to refine our models and test our predictions.

Dendrimer-encapsulated nanoparticles (DENs) provide an excellent model system which can be synthesized and characterized at the atomic scale for direct comparison with theory. DENs are synthesized by sequestering metal ions within the interior of, for example, poly(amidoamine) (PAMAM) dendrimers, followed by chemical reduction of the metal-ion/dendrimer complex with a reducing agent such as borohydride. [2–5] Two features of DENs make them a good model system for correlating theory and experiment. First, their size, composition, and structure can be precisely controlled. [6,7] Second, the dendrimers stabilize the encapsulated nanoparticles and provide a handle for linking them to an electrode surface, but they do not interfere significantly with reactions on the particle surface. [8]

Fig. 1 illustrates the synthetic routes to form random alloy [9,7,10–12], core-shell [13–16], and alloy-core@shell DENs [17]. Random alloy DENs are prepared by a co-complexation method, where two types of metal cations are reduced simultaneously to form an alloy particle. Core@shell nanoparticles are produced by a sequential reduction or underpotential deposition (UPD) of a shell metal onto the core. Galvanic exchange, which is also known as redox displacement, is an elegant technique which can then be used to replace reactive elements in the DENs with more noble ones, [18] increasing the variety of shells that are available for the DENs synthesis.

Alloy nanoparticles have a broad range of applications for many catalytic processes. In this paper we focus on the oxygen reduction reaction (ORR). The ORR is the cathode reaction of proton-exchange membrane fuel cells. It involves at least two elementary processes, O_2 dissociation and the subsequent removal of the dissociated species by further reduction to H_2O. ORR activity can be measured experimentally using electrochemical techniques, including cyclic voltammetry (CV) and rotating disk voltammetry (RDV). Theoretically, the ORR activity of a surface is understood to correlate with the O binding energy. Pioneering work by Nørskov and co-workers have established a volcano-shaped correlation between the O binding energy and ORR activity. [20,21] On the strong-binding side of the volcano, oxygen species over-bind to the catalyst surface and limit the kinetics of product formation. On the weak-binding side of the volcano the reaction is limited by oxygen dissociation and adsorption. Pt offers the optimal tradeoff of the pure metals and the peak of the volcano corresponds

* Corresponding author.
E-mail address: henkelman@utexas.edu (G. Henkelman).

http://dx.doi.org/10.1016/j.susc.2015.03.018
0039-6028/

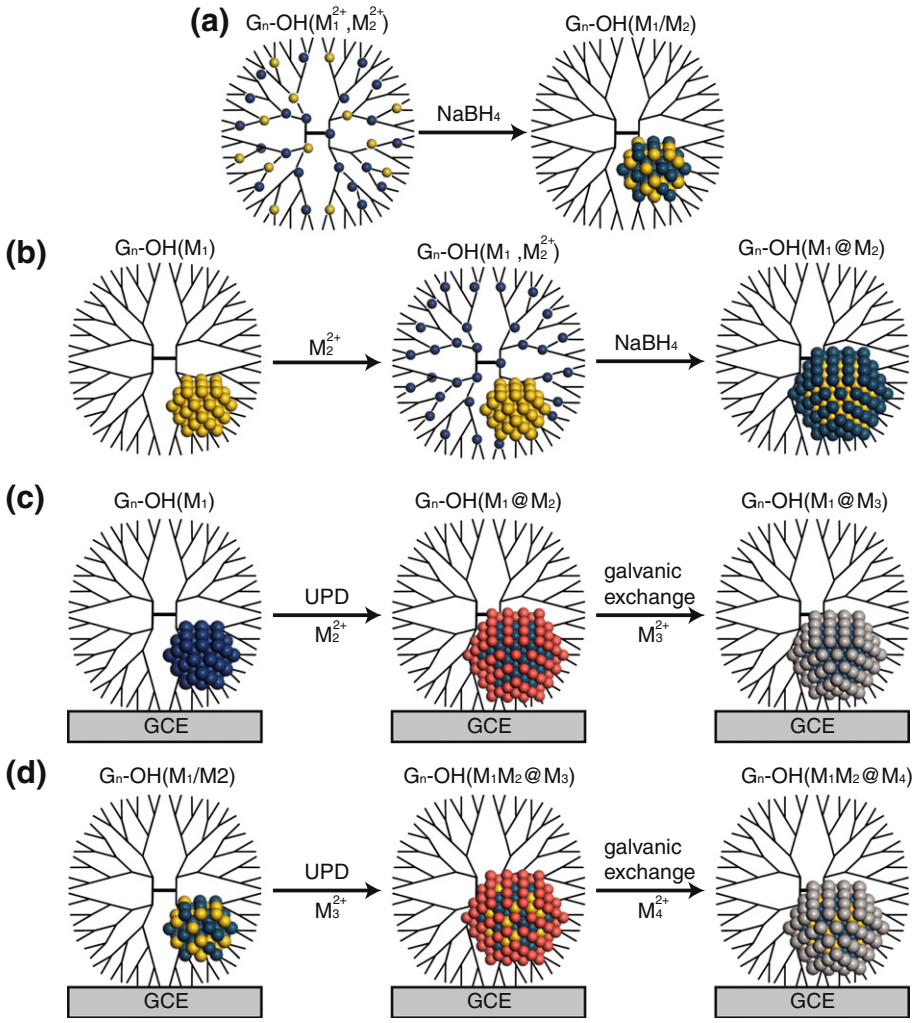

Fig. 1. Routes to synthesize different metallic DENs, including: (a) random alloy, (b) core@shell via sequential reduction, (c) core@shell and (d) alloy-core@shell via underpotential deposition and subsequent galvanic exchange.

to an oxygen binding energy which is slightly weaker than on a Pt(111) surface. The underlying reason that oxygen binding is a good reactivity descriptor is that there is a Brønsted-Evans-Polanyi (BEP) correlation between the binding and transition state energies, so that a single descriptor can describe both limits. In Fig. 2, Tang *et. al.* show the BEP relationship between the O_2 dissociation barrier and O binding energy for a 79 atom Pd-shelled nanoparticle (NP79) and single-crystal (111) transition metal surfaces. [19] Thus a similar trade off between the dissociation barrier and weak product binding is expected for ORR on (111) facets of small sized nanoparticles.

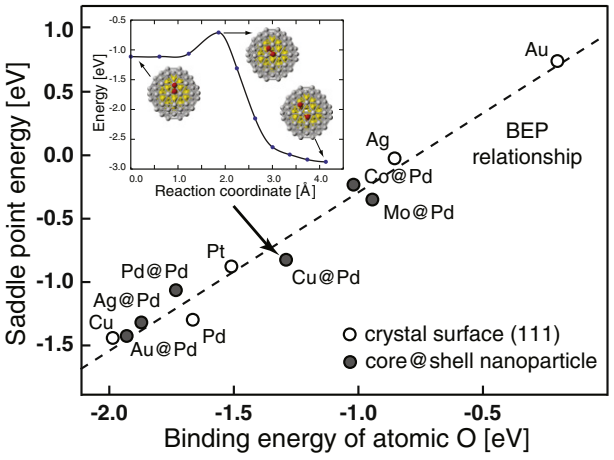

Fig. 2. The saddle point energy for oxygen dissociation on Pd-shelled particles and single-crystal surfaces plotted as a function of O binding energy. The linear trend is a BEP relationship. Particles with barriers and binding energies near Pt(111) are promising catalysts for the ORR. Reproduced with permission from Ref. [19].

In the following, we consider several nanoparticle alloys and seek to find structures with oxygen binding energies, and hence ORR activities, that approach or exceed that of Pt.

2. Random Alloy Nanoparticles

The random alloy structure is one of the most conventional forms of bimetallics, where two elements are randomly or nearly randomly dispersed in the material. Random alloy DENs can be synthesized by the aforementioned co-reduction method shown in Fig. 1(a). A number of random alloys DENs, including Pd/Au, Pd/Cu, Pd/Pt and Au/Ag, in the size range of 1–2 nm have been successfully synthesized. [11,10,7,12,9], The catalytic properties of a random alloy nanoparticle can be tuned by adjusting the ratio of the component elements. Studies on large particles (which behave similarly to bulk) have revealed that adding small amounts of metals which bind oxygen strongly (e.g. Co, Ni and Cu) can weaken the oxygen binding to more noble metals (Pt or Pd) and improve their ORR activity. [22–25]

2.1. Geometric Effects in Pd/Pt random alloy NP79

Fig. 3(a) shows the experimentally measured ORR activity of Pd/Pt DENs as a function of composition. [7] An enhancement of ORR activity was observed by the addition of small amounts of Pd to a Pt DEN. The average oxygen binding energy was calculated using DFT for Pd/Pt random alloys in a slab and NP79 geometry as a function of Pd/Pt composition. [26] A nearly linear binding energy trend is found for Pd/Pt slabs with increasing Pt ratio. However when the nanoparticle size is reduced to 79 atoms, the linear trend develops curvature and has a maximum activity at Pd:Pt of 1:1. Moreover, this nonlinear trend disappears when the NP79 structure is frozen in its structure before oxygen binding, indicating the important role of geometry relaxation in determining the catalytic activity of small alloy nanoparticles (see Fig. 3(b)) To better understand this geometric relaxation effect, the total binding energy E_{tot} was decomposed into two parts, (i) the oxygen affinity E_a calculated as the oxygen binding energy to the frozen particle, and (ii) the subsequent energy of the geometric relaxation E_d of the particle due to the presence of bound oxygen. This energy decomposition, shown in Fig. 3(c,d), shows that E_a is insensitive to geometry whereas E_d is strongly size dependent. The value of E_d becomes comparable to E_a for the 79-atom nanoparticle, for which structural relaxation is much easier than in a slab geometry. The curvature of E_d is a consequence of Pt-Pt bonding, which varies quadratically with the fraction of Pt atoms in the particle, [26] and is key to understanding why Pt/Pd alloys are more active than either pure Pt or Pd nanoparticles.

The structural deformation of Pt nanoparticles induced by atomic oxygen binding stabilizes oxygen species bound to the surface and causes Pt NP79 to over-bind oxygen and reduce the ORR activity. We describe these properties of Pt (and also Au) as being soft with respect to oxygen binding. Our calculations show that introducing a harder element (Ag, Cu or Pd) disrupts the Pt-Pt bonding so that the particle resists deformation upon oxygen adsorption which in turn reduces the over-binding and increases ORR activity.

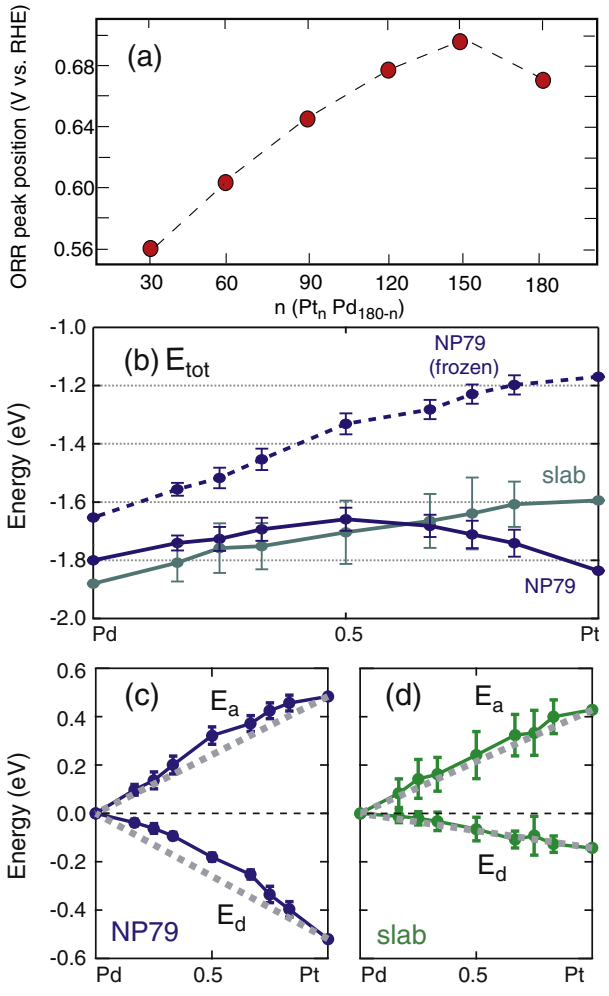

Fig. 3. (a) Experimental ORR peak current position for various Pt_nPd_{180-n} compositions (reproduced from Ye and Crooks [7]). (b) The average oxygen binding energy as a function of Pd/Pt alloy composition, with error bars indicating the standard deviation over random alloy structures. An activity maximum is seen at an intermediate composition for the NP79 structure. This maximum is due to a geometric relaxation of the surface atoms because it is not present in the slab geometries or when the NP79 structure is held frozen upon oxygen binding. The total oxygen binding energy and the energy decomposition of the Pd/Pt random alloy in the forms of (c) NP79 and (d) slab at various compositions. For ease of comparison, all of the curves were shifted to zero at the left. The grey dashed lines represent the linear interpolations from the pure metal data. Reprinted (adapted) with permission from Ref. [26]. Copyright (2011) American Chemical Society.

While geometric relaxation is important to understand the ORR activity trend of Pd/Pt random alloy nanoparticles, electronic effects are dominant in random alloy nanoparticles formed by two hard elements, such as Pd and Cu. Geometric and electronic effects were studied to determine their contributions for tuning the oxygen binding. The geometric effect is independent of the Cu ratio, and therefore only the electronic effect is responsible for the oxygen binding trend. The oxygen binding energy trend of Pd/Cu random alloy NP79 was studied for a range of compositions (Cu% = 0, 0.25, 0.5, 0.75 and 1), as shown in Fig. 4. [27] Although Cu NP79 itself binds oxygen more strongly than Pd NP79, the addition of Cu to Pd initially weakens the average oxygen binding until it reaches the extremum at Pd:Cu ratio of 1:1. While all the Pd/Cu random NP79 alloys bind oxygen more strongely than Pt(111) (dashed line in Fig. 4), the highest ORR activity should be achieved at the weakest oxygen binding composition, that is a Pd:Cu ratio near 1:1. This optimal ratio from our calculation matches well with previous experiments, where Cu has been found to promote the ORR activity of Pd at a ratio of 50%. [28,29]

When Cu is alloyed into Pd, charge shifts from Cu to Pd since Cu has a higher Fermi level. This charge redistribution lowers the Pd *d*-band and raises the Cu *d*-band. Thus, the Cu atoms neighboring Pd decrease the Pd-O bond strength, while Pd atoms neighboring Cu increase Cu-O binding. These effects are not symmetric, however, as shown in Fig. 5, where the oxygen binding was decomposed into Pd-O and Cu-O interactions as a function of the Cu ratio according to the *d*-band model.

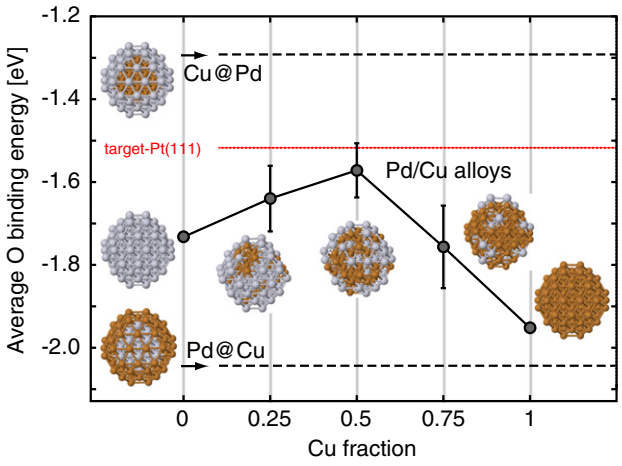

Fig. 4. Average binding energy of oxygen on alloy Pd/Cu nanoparticles, with error bars indicating the standard deviation of 80 binding sites with different random alloy structures. Using this binding energy as a reactivity descriptor for the ORR indicates a peak in activity for random alloy particles at 1:1 compositions of Cu (dark color) and Pd (light color). Reprinted with permission from Ref. [27]. Copyright (2011) American Chemical Society.

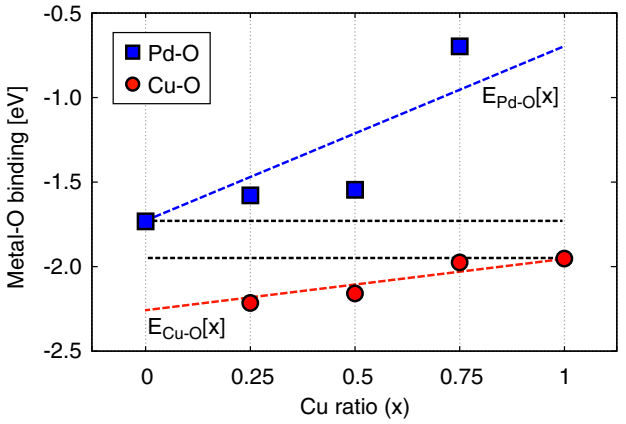

Fig. 5. Pd-O binding (blue squares) and the Cu-O binding (red circles) for alloy particles with different ratios of Cu. The Cu-O binding changes by a small amount, whereas the Pd-O binding is largely reduced by the addition of Cu. Reprinted with permission from Ref. [27]. Copyright (2011), American Chemical Society.

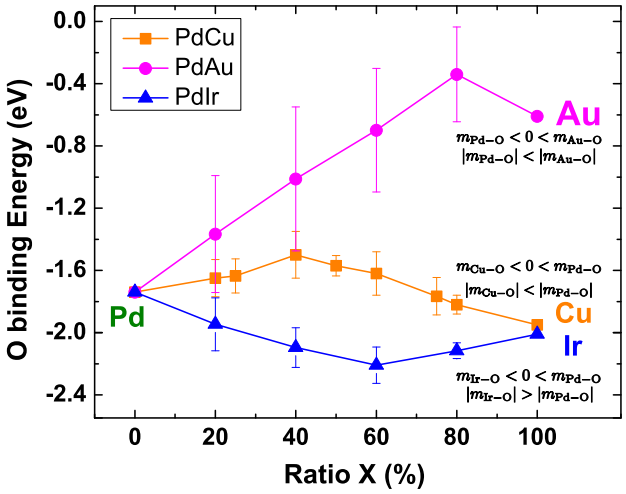

Fig. 6. The average O binding energy trend of Pd/X (X = Au, Cu, Ir) random alloy with different ratio of X in the particles.

[30] The slope of the Pd-O interaction, m_{Pd-O}, is larger in magnitude than the Cu-O slope, m_{Cu-O}. In other words, the alloying of Pd and Cu weakens the Pd-O interaction more than it strengthens the Cu-O interaction. The average binding to an alloy particle can be written as a linear combination of Pd-O and Cu-O interactions, weighted by the fraction of each metal in the particle. The Pd-O and Cu-O interactions can be estimated as a linear function of composition using the slopes m_{M-O},

$$\begin{aligned} E_b[x] &= (1-x)\ E_{Pd-O}[x] + x\ E_{Cu-O}[x] \\ &= (1-x)\ \left(E^0_{Pd-O} + x\ m_{Pd-O}\right) \\ &\quad + x\ \left(E^0_{Cu-O} + (1-x)\ m_{Cu-O}\right) \\ &= (1-x)\ E^0_{Pd-O} + x\ E^0_{Cu-O} \\ &\quad + \left(x - x^2\right)\ (m_{Pd-O} + m_{Cu-O}), \end{aligned} \tag{1}$$

where x is the composition of Cu and E^0_{M-O} is the binding to a pure particle of metal M. In the final expression, the first two terms are linear interpolations between the binding at the pure metal particles, and the last term is a quadratic function that describes the relative change in binding due the metals' influence on each other. The difference in magnitude of m_{Pd-O} and m_{Cu-O} gives rises to the nonlinear binding trend with a curvature towards weak binding at intermediate compositions.

We expect the above non-linear binding trend to be a general property of adsorbate binding to random alloys, providing a prescription for tuning catalytic activity through alloying. The curvature is determined by the sign and relative magnitude of m_{M-O}, which can be estimated from the oxygen binding energy on core@shell nanoparticles. As shown in Fig. 6, Pd/X (X = Au, Cu, Ir) random alloy NPs all exhibit non-linear oxygen binding trends. The oxygen binding trend for Pd/Ir alloys has the opposite curvature of Pd/Cu and Pd/Au. This can be understood by considering, for example, the Pd/Au alloy. Au has a lower Fermi level than Pd so charge transfers from Pd to Au when they are alloyed. Table 1 shows that replacing the core of Pd@Pd with Au enhances the O binding while Pd@Au binds O more weakly than Au@Au. Thus, m_{Pd-O} is negative and m_{Au-O} is positive. Furthermore, $|Eb_{Au@Pd} - Eb_{Pd@Pd}| < |Eb_{Pd@Au} - Eb_{Au@Au}|$ so that the magnitude of m_{Au-O} is larger than m_{Pd-O}. Therefore, the oxygen binding trend of Pd/Au has a negative curvature since $-(m_{Pd-O} + m_{Au-O}) < 0$ (see Fig. 6). A similar argument can also be applied to the Pd/Cu and Pd/Ir systems. In the Pd/Cu system, $m_{Pd-O} > 0$, $m_{Cu-O} < 0$ and $|m_{Cu-O}| < |m_{Pd-O}|$, the oxygen binding trend shows a negative curvature. While, in Pd/Ir random alloy nanoparticles, $m_{Pd-O} > 0$, $m_{Ir-O} < 0$ and $|m_{Ir-O}| > |m_{Pd-O}|$ giving rise to a positive curvature.

3. Core-shell Nanoparticles

Core@shell nano-structures are important because they exhibit tunable properties arising from the influence of a core metal on the shell. [19,31–34] This phenomenon has been applied to electrocatalytic [32,33,35] and spectroscopic applications [34], Early examples demonstrating the importance of Pt-shell nanoparticles as active electrocatalysts for the ORR were reported by Adzic and coworkers. [32,33] The relationship between bimetallic nanoparticle structure and catalytic activity has been correlated to DFT calculations by a number of groups. [36,37,35,38]

Preparation of core-shell DENs is typically achieved by sequential synthesis, as illustrated in Fig. 1(b,c). In the first step, the core is prepared by homogeneous reduction of a dendrimer/metal ion monometallic precursor. After that, shell atoms are formed on the core cluster by either chemical reduction or UPD. Chemical reduction results in less control of the shell thickness but is able to cover low-coordinated sites (corner/edge) that are usually considered exposed in UPD. UPD provides a systematic scheme to generate a well-defined monolayer shell. [39–41] In order to have UPD of metal M_1 onto M_2, M_1 should have stronger interaction with M_2 than with itself. Thus under a certain applied voltage, deposition of M_1 occurs exclusively on M_2. Since different crystallographic planes of DENs give rise to UPD waves at different electrochemical potentials, UPD complemented with extended X-ray absorption fine structure (EXAFS) spectroscopy and DFT simulation can be used to tune the shell structure of DENs. Below, we show examples of correlating experiment and DFT in understanding the structures and catalytic function of core@shell nanoparticles.

3.1. Pb UPD on Au_{147}

The Au_{147} DENs were modeled as cuboctahedral particles having (100) and (111) facets. [15] DFT calculations indicate that Pb UPD occurs on the (100) facet before the (111) facet. The average adsorption energy of Pb on (100) was found to be 0.1 eV per Pb atom stronger than on the (111) facet, showing that Pb adlayers on Au_{147}(100) are more stable than those on Au(111). Additionally, an atom-by-atom

Table 1
Oxygen Binding Energy (eV) of Core-shell NPs for Pd/Au, Pd/Cu and Pd/Ir systems.

Eb_O(eV)	Pd@Pd	X@Pd	X@X	Pd@X	X@Pd-Pd@Pd	Pd@X-X@X
Pd/Au	−1.73	−2.03	−0.60	0.05	−0.30	0.65
Pd/Cu	−1.73	−1.31	−1.95	−2.04	0.42	−0.09
Pd/Ir	−1.73	−1.56	−2.01	−2.33	0.17	−0.32

deposition of Pb onto Au_{147} was modeled with DFT. $E_{ad}(n)$, the energy required to successively add the n^{th} Pb atom to the surface of Au_{147}, was referenced to the binding energy of Pb on a bulk Pb surface. A theoretical UPD potential for each deposition event was then calculated as,

$$V_{Pb}^{DFT} = V_{Pb\text{-}bulk}^{Exp} - \frac{1}{2}E_{ad}(n). \quad (2)$$

Here $V_{Pb-bulk}^{Exp}$ is the experimentally measured Pb bulk deposition potential (− 0.90 V vs Hg/Hg_2SO_4), and the factor of 1/2 accounts for the two-electron Pb deposition and stripping process. Fig. 7 provides an overlay of a Pb UPD voltammogram and the energy for deposition and stripping of Pb calculated by DFT. Good agreement is observed between the CV and the calculated histogram of Pb adsorption energies. The potentials of the two most prominent Pb stripping peaks, measured using the Au_{147}-modified electrode, are at − 0.69 and − 0.54 V, where DFT simulation shows stripping events on (111) at − 0.75 V and (100) at − 0.54 V. All of these observations are consistent with our contention that Au_{147} DENs have a cuboctahedral structure, where the (100) and (111) facets are present while (110) facets are absent. The assignment of the UPD peaks provides the appropriate voltages for preparation of core@shell particle with only certain facets covered. By holding the voltage at − 0.85 and − 0.63 V, Au@Pb with complete shell (both (100) and (111) covered) and partial shell (only (100) covered) can be synthesized, as illustrated by the structures shown in Fig. 7.

3.2. Cu UPD on Pt_{147}

In a related study, we aimed to cover specific facets of Pt DENs using Cu UPD. [13,42] The same cuboctahedral structure was used to model the Pt_{147} DENs. Similarly to Pb on Au, Cu atoms are preferentially deposited on Pt(100) facets first and then on the Pt(111) facets. The Cu stripping process was exactly the opposite of the deposition, with Cu from the Pt(111) facet desorbing first. A similar DFT calculation of the UPD potential was performed for Cu on Pt, yet the computed binding energies of Cu to the Pt nanoparticles (in vacuum) did not match those observed in the experiments. However, by considering the competitive binding of the SO_4 counter ions (present in the electrolyte) for the Pt@Cu DENs, the theoretical results lined up much better with experiment.

Fig. 8 shows the calculated potentials for Cu UPD and stripping with and without SO_4 adsorbed to the Pt DEN surface. The calculated results

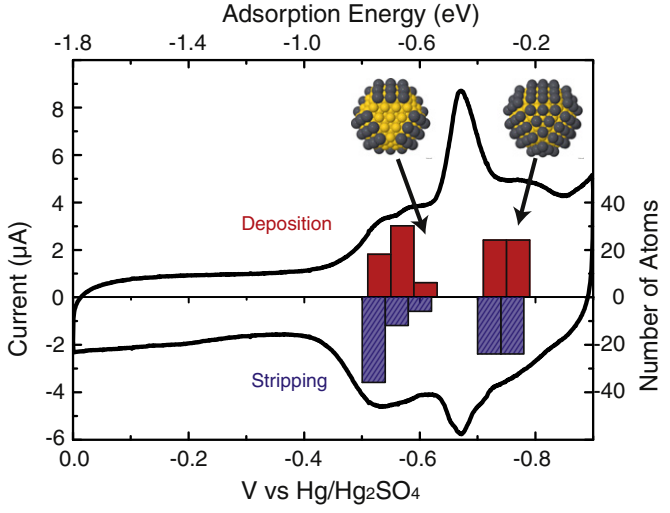

Fig. 7. Cyclic voltammetry showing the Pb UPD process at a Au_{147} DEN-modified glassy carbon electrode. The DFT-calculated potentials for Pb deposition (red bars) and stripping (blue bars) are also shown. Reproduced from Ref. [15] by permission of The Royal Society of Chemistry.

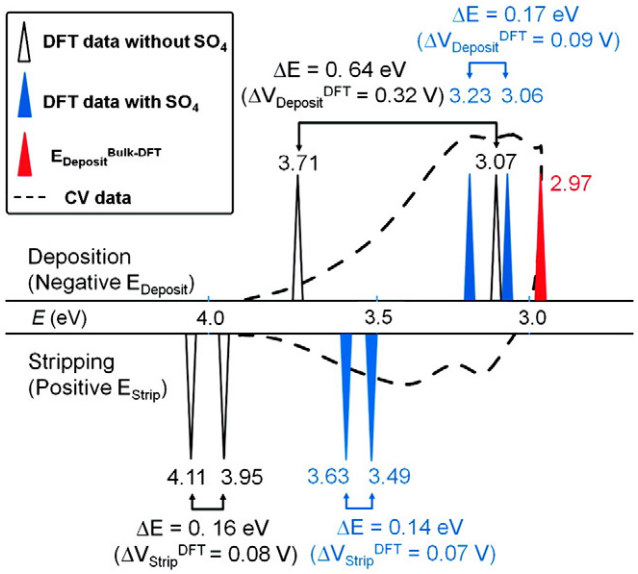

Fig. 8. DFT calculated Cu deposition and stripping energies for the various models with the experimentally obtained Cu UPD CV overlaid for comparison (black dashed line). Reprinted (adapted) with permission from Ref. [42]. Copyright (2012) American Chemical Society.

are overlaid onto an experimental voltammogram. In the presence of SO_4 ligands, Cu atoms exhibit a weakened interaction with Pt(100) as compared to bare Pt_{147}. The UPD shifts for Cu stripping are calculated to be 0.33 and 0.25 V for the Pt(100) and Pt(111) facets, respectively. These potentials are much closer to the corresponding experimentally observed UPD shifts of 0.29 and 0.15 V, illustrating the importance of ligand interactions in this system.

3.3. $Au_{147}@Pt_{54}$ and $Au_{147}@Pt_{102}$

Au_{147}@Pt (core@shell) DENs were synthesized by transferring the aforementioned $Au_{147}@Pb_{54}$ and $Au_{147}@Pb_{102}$ DEN-functionalized electrode into a solution of Pt^{2+}. [15] This operation results in galvanic exchange of the Pb UPD shells for Pt, and conversion of the Au_{147}@Pb DENs to Au_{147}@Pt DENs. The amount of Pb deposited by UPD determines the amount of Pt on the particle surface. The relaxed structure of Au_{147}@Pt DENs having a complete Pt shell (111 and 100 facets covered) and a partial Pt shell (just the 100 facets covered) were calculated using DFT (Fig. 9(a)). Subsequently, the relaxed structures were used as starting points for DFT molecular dynamics (MD) simulations. These were carried out at 350 K over 10 ps and showed that surface Pt covering the (100) facet of the Au particle distorted into a (111)-like diamond configuration. The diamond structure is − 0.2 eV/Pt atom more favorable than the nine atom square Pt(100) facet.

Au_{147}@Pt DENs having partial and full Pt shells were investigated as electrocatalysts for the ORR. Fig. 9(b) shows that Au_{147}@Pt DENs having partial and full shells had specific activities (at 0.65 V vs. RHE) of 2.70 and 2.84 mA/cm^2, respectively; a difference of only 5%. The similarity in activity for the ORR is supported by oxygen binding calculations on the diamond shaped Pt(111) surfaces, as illustrated in Fig. 9(c). On a Pt(111) facet from the partially decorated particle, the oxygen binding energy is − 1.03 eV and on a Pt(111) facet from the fully covered particle, the oxygen binding energy is − 1.01 eV. This correlates the experimental finding that the extent of Pt surface coverage does not significantly change the activity of the particles for the ORR. The compressed diamond Pt facets have promising catalytically active sites for reactions where conventional Pt may be poisoned by intermediates, *e.g.* CO. For example, Iyyamperumal *et. al* reported an enhanced electrocatalytic activity of formic acid oxidation on this Au_{147}@Pt DEN structure where the deformed Pt facets with a compressed Pt-Pt bonds

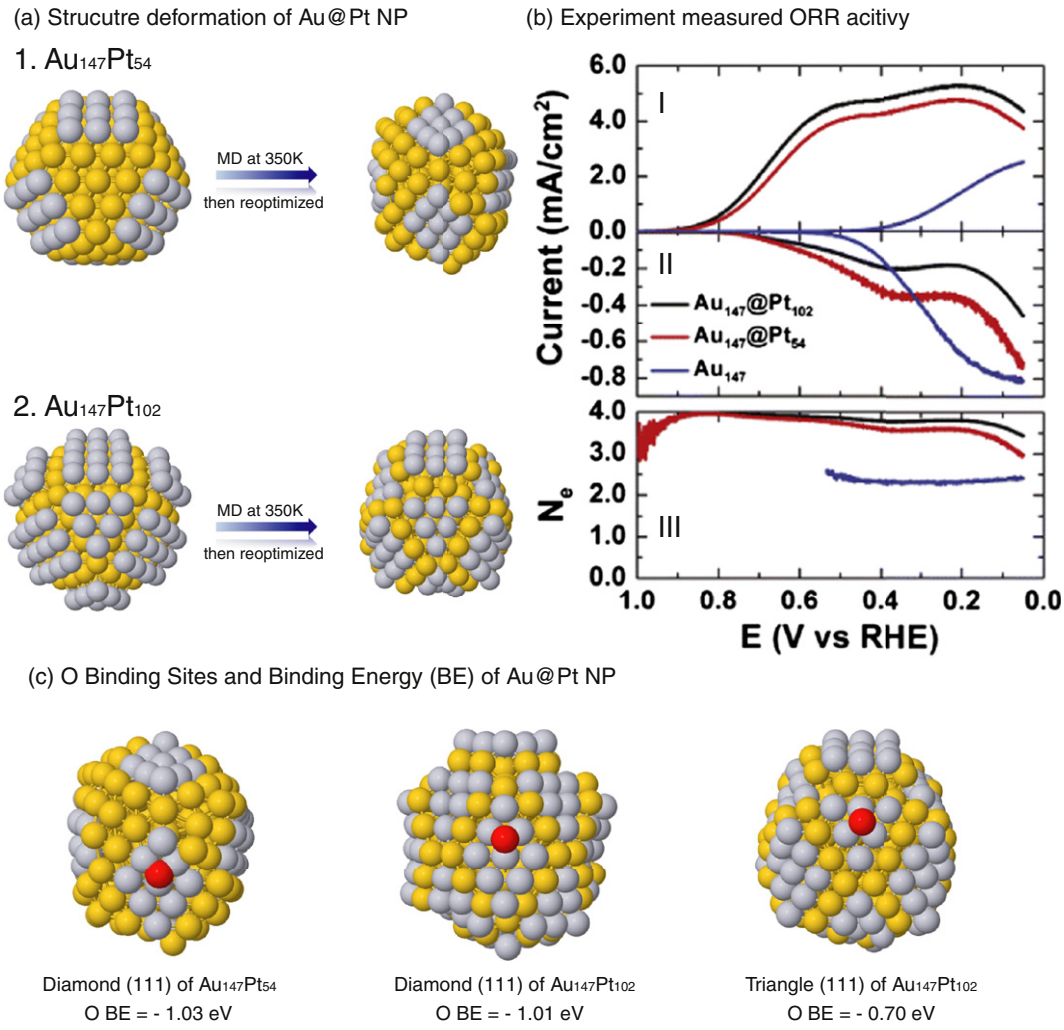

Fig. 9. (a) DFT-calculated structures for Au_{147}@Pt_{54} and Au_{147}@Pt_{102} DENs. (bI) ORR polarization curves for the indicated DEN-modified glassy carbon electrodes. (bII) Ring currents arising from the oxidation of peroxide generated at the disk electrode during the ORR. (bIII) The apparent number of electrons calculated from the disk and ring currents. The electrolyte solution was O_2-saturated 0.10 M $HClO_4$, the scan rate was 20 mVs^{-1}, and the rotation rate was 1600 RPM. (c) Oxygen binding sites and energies for Au_{147}@Pt_{54} and Au_{147}@Pt_{102} DENs. Reproduced from Ref. [15] with permission of The Royal Society of Chemistry.

suppress the indirect pathway of formic acid oxidation and largely reduces the CO poisoning. [43]

4. Alloy-core@shell Nanoparticles

As shown in the previous two sections, random-alloy and core@shell are two structures that have been well-studied to search for bimetallic catalysts. They are often studied because of the opportunity to tune electrocatalytic properties by controlling the structure of the particles. However, there are some shortcomings of these two structures from the viewpoint of particle synthesis and design. Variations in the core@shell structures are discrete in chemical compound space (elements can only be changed by integer atomic numbers) so that the properties of such particles can not be tuned precisely. As shown in Fig. 2, none of the single core@Pd NP79 achieve the same oxygen binding as Pt(111).

The properties of the random alloy structure, on the other hand, can be finely tuned by varying the composition of the components. However the presence of reactive metals on the surface of the alloy nanoparticle could be unstable under reaction conditions and dissolve into solution. The combined alloy-core@shell structure aims to take advantage of the strengths of the alloy and core@shell particles, and avoid their flaws. Noble metal shells (e.g. Pt, Pd) are stable during synthesis and characterization, and the alloy core offers the opportunity to tune the electronic and geometric properties of the shell by changing its composition. Similar structures have been studied by the Stamenkovic and Adzic groups. [23,44,45] In this section, we show how the catalytic properties of alloy-core@shell particles are tuned by the core composition. The predictive power of first principles theory in leading the design cycle for novel materials is also demonstrated here for the ORR.

4.1. Linear binding correlation of alloy-core@shell nanoparticles

The average oxygen binding energy at Pd/X (X = Ir, Rh, Cu, Ru and Mo) alloy core with Pd shell nanoparticles are studied as a function of the ratio of metal X in the alloy core, as shown in Fig. 10(a). [46] The red dashed line marks the oxygen binding on Pt(111), which is chosen as the target value. X@Pd (X = Ir, Rh, Cu, Ru and Mo) bind oxygen too strongly as compared to Pt(111), while Cu@Pd binds oxygen too weakly – they are on the opposite branches of the volcano plot. All of these particles are expected to have lower activity as compared with Pt(111). Our calculations show that the oxygen binding energy can be weakened linearly by mixing Cu into these cores. As demonstrated in Fig. 10(b-d), this linear binding correlation is independent of types of core or shell metals, adsorbate molecules, size of particles, thereby providing a general description for tuning principle of alloy-core@shell nanoparticles. [17,47]

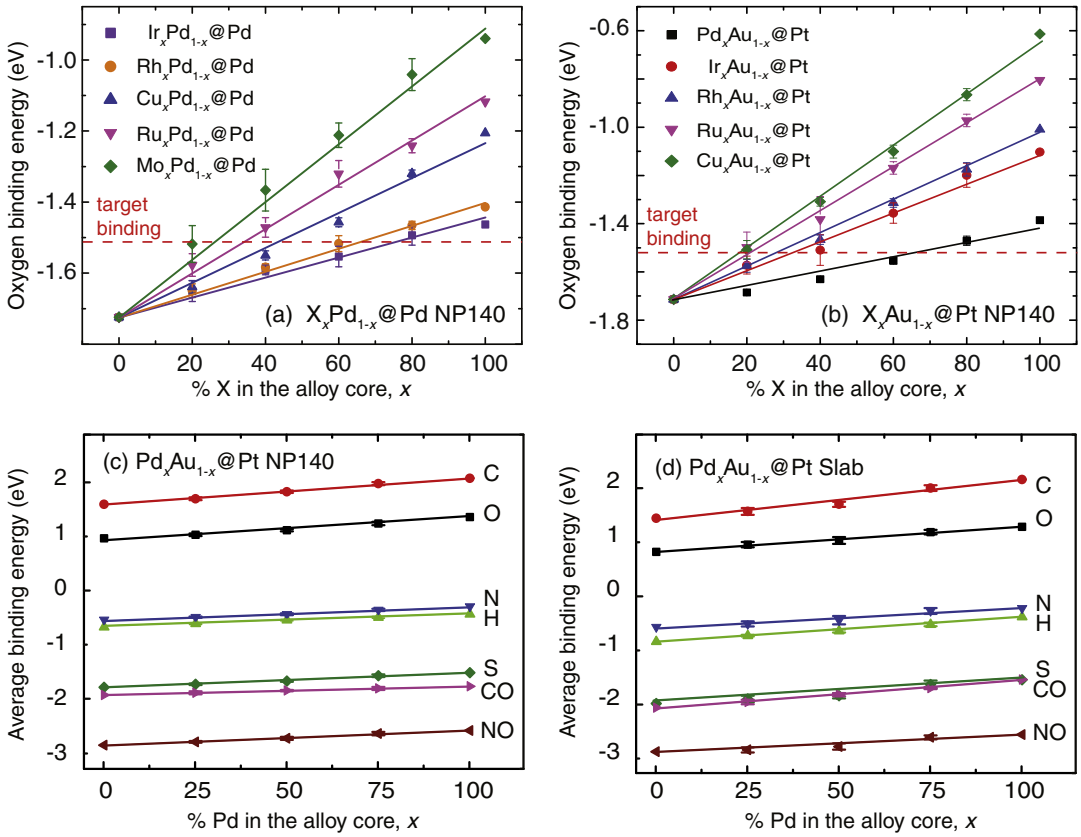

Fig. 10. (a) Oxygen binding on X_xPd_{1-x}@Pd NP140 (X = Ir, Rh, Cu, Ru and Mo). Reprinted (adapted) with permission from Ref. [46]. Copyright (2012) American Chemical Society. (b) Oxygen binding on X_xAu_{1-x}@Pt NP140 (X = Pd, Ir, Rh, Ru and Cu. Reprinted (adapted) with permission from Ref. [17]. Copyright (2013) American Chemical Society. (c) Average binding trends of seven different adsorbates (C, O, N, H, S, CO and NO) on Pd_xAu_{1-x}@Pt NP140 and (d) Pd_xAu_{1-x}@Pt slab. Linear correlations between the binding of adsorbates to the shell and the alloy core composition of alloy-core@shell NP are found, regardless of the shell metal (a, b), the core metals combination, or the adsorbate molecules and size (c, d).

For alloy-core@shell nanoparticles X_xY_{1-x}@Z, the binding energy can be estimated from a linear combination of two single-core@shell nanoparticles X@Z and Y@Z by,

$$Eb(x) = xEb_{X@Z} + (1-x)Eb_{Y@Z}. \quad (3)$$

This linear tuning mechanism offers a new scheme for catalyst design. Taking the ORR for example, the target oxygen binding energy of X_xY_{1-x}@Z can be achieved by alloying a metal X and Y, where X@Z and Y@Z are on the opposite sides of the target value. The optimal ratio x* for X_xY_{1-x}@Z to achieve target binding is given by,

$$x^* = \frac{Eb^* - Eb_{Y@Z}}{Eb_{X@Z} - Eb_{Y@Z}}, \quad (4)$$

where Eb^* is the target binding.

4.2. Pd/Au@Pt for ORR catalyst

Following the above design principle, several alloy-core compositions with a Pt shell emerge as good ORR catalysts. The optimal compositions can be obtained from Fig. 10(b). One such promising structure is $Pd_{0.72}Au_{0.28}$@Pt. Based on our theoretical prediction, we synthesized a series of PdAu@Pt DENs with different Pd:Au ratios in the alloy core, as illustrated in Fig. 1(d). The Pd/Au random alloy core was prepared by co-reduction. Then Cu UPD was conducted on the Pd/Au random alloy DENs modified electrode to form a homogenous Cu shell. Finally, Pd/Au@Pt DENs were then synthesized by a subsequent galvanic exchange, replacing the Cu shell with Pt. [17]

The ORR activity of these PdAu@Pt DENs was determined using RDV, by measuring the onset potential where the current density reached 0.1 mA/cm^2. [17] Fig. 11(b) plots the RDV measured ORR onset potential against the corresponding oxygen binding energy calculated from DFT, exhibiting a volcano-like activity trend. Notably, data for Pd@Pt DENs is not shown on Fig. 11 because there was core/shell inversion, which was confirmed by EXAFS and DFT.[16] Alloying Au to the Pd-core not only optimized the catalytic activity but also enhanced its stability. The peak activity was achieved with 75% Pd in the core, in perfect agreement with our prediction from the linear binding model. As shown in the above section, this linearly tuning mechanism is a general property of alloy-core@shell nanoparticles. Therefore, similar catalyst design scheme based on alloy-core@shell nanoparticles is expected to be transferable to other important catalytic processes.

5. Conclusions

We systematically studied structure-function relationships on alloy DENs having random alloy, core@shell and alloy-core@shell structures. For random alloy nanoparticles, we found that geometric and electronic effects play an important role in the oxygen binding trend of Pd/Pt and Pd/Cu random alloy NP79, respectively. The oxygen binding trend of Pd/Pt consistent with that observed experimentally. In the case of core@shell nanoparticles, theory and experiment were coupled together to understand the structure and their corresponding catalytic performance. Partial shell nanoparticles have a significant portion of their surface made up of bimetallic interfaces. By choosing appropriate pairs of metals, these interfacial sites can be designed to avoid competition between adsorbate binding of reactants, leading to a high activity. [48] Distortion of Pt facets on Au@Pt DENs were found to aid in reducing Pt poisoning. For alloy-core@shell nanoparticles, novel structures were proposed first theoretically and then subsequently tested experimentally. The close correlation between theory and experiment is shown to

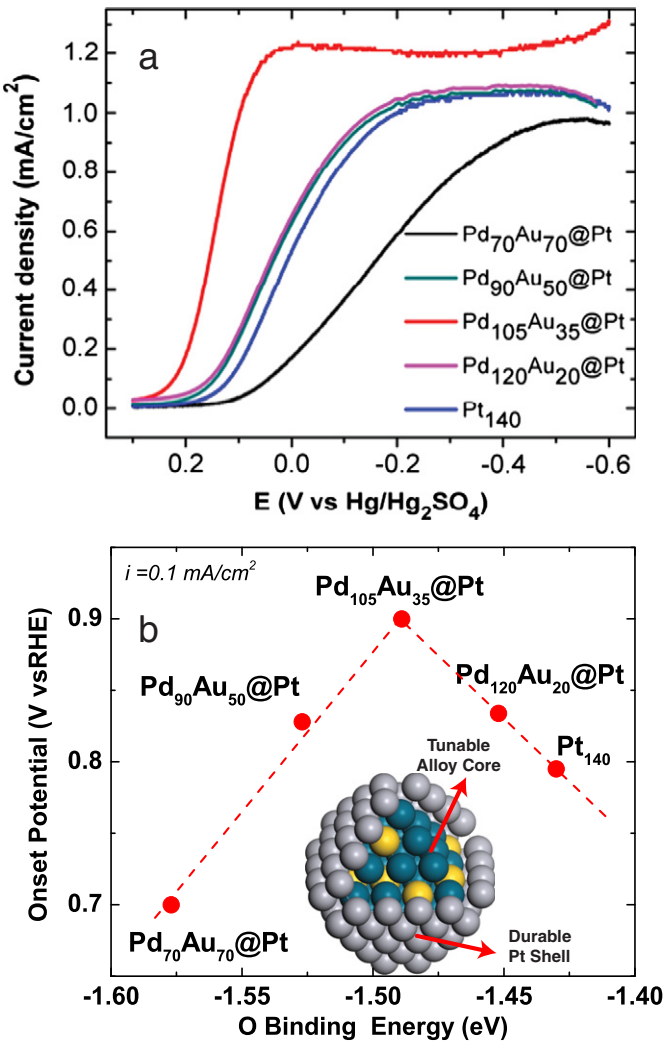

Fig. 11. (a) Rotating disk voltammograms for glassy carbon electrodes modified with Pd_nAu_{140-n}@Pt(n = 70, 90, 105, 120) and Pt_{140} DENs. (b) Onset potential for the ORR at Pd_xAu_{1-x}@Pt DENs measured by RDVs and plotted as a function of the corresponding oxygen binding energy calculated by DFT. Reprinted (adapted) with permission from Ref. [17]. Copyright (2013) American Chemical Society.

facilitate the understanding of nanoparticle catalysis and reduce the effort involved in the development cycle of promising new catalysts.

Acknowledgments

This work was supported by the Chemical Sciences, Geosciences, and Biosciences Division, Office of Basic Energy Sciences, Office of Science, U.S. Department of Energy (Contract DE-FG02-13ER16428). Computing time was provided by the National Energy Research Scientific Computing Center and the Texas Advanced Computing Center.

References

[1] M. Haruta, M. Daté, Appl. Catal., A 222 (2001) 427.
[2] D. Yamamoto, S. Watanabe, M.T. Miyahara, Langmuir 26 (4) (2010) 2339.
[3] R.W.J. Scott, O.M. Wilson, R.M. Crooks, J. Phys. Chem. B 109 (2) (2005) 692.
[4] H. Lang, R.A. May, B.L. Iversen, B.D. Chandler, J. Am. Chem. Soc. 125 (48) (2003) 14832.
[5] M. Bernechea, S. García-Rodríguez, P. Terreros, E. de Jesús, J.L.G. Fierro, S. Rojas, J. Phys. Chem. C 115 (4) (2011) 1287.
[6] H. Ye, J.A. Crooks, R.M. Crooks, Langmuir 23 (23) (2007) 11901.
[7] H. Ye, R.M. Crooks, J. Am. Chem. Soc. 129 (12) (2007) 3627.
[8] H. Ye, R.M. Crooks, J. Am. Chem. Soc. 127 (13) (2005) 4930.
[9] O.M. Wilson, R.W.J. Scott, J.C. Garcia-Martinez, R.M. Crooks, J. Am. Chem. Soc. 127 (2005) 1015.
[10] M.R. Knecht, M.G. Weir, A.I. Frenkel, R.M. Crooks, Chem. Mater. 20 (3) (2008) 1019.
[11] M.G. Weir, M.R. Knecht, A.I. Frenkel, R.M. Crooks, Langmuir 26 (2) (2010) 1137.
[12] S.V. Myers, A.I. Frenkel, R.M. Crooks, Chem. Mater. 21 (20) (2009) 4824.
[13] E.V. Carino, R.M. Crooks, Langmuir 27 (2011) 4227.
[14] D.F. Yancey, E.V. Carino, R.M. Crooks, J. Am. Chem. Soc. 132 (2010) 10988.
[15] D.F. Yancey, L. Zhang, R.M. Crooks, G. Henkelman, Chem. Sci. 3 (2012) 1033.
[16] R.M. Anderson, L. Zhang, J.A. Loussaert, A.I. Frenkel, G. Henkelman, R.M. Crooks, ACS Nano 7 (10) (2013) 9345.
[17] L. Zhang, R. Iyyamperumal, D.F. Yancey, R.M. Crooks, G. Henkelman, ACS Nano 7 (10) (2013) 9168.
[18] J. Zhang, Y. Mo, M.B. Vukmirovic, R. Klie, K. Sasaki, R.R. Adzic, J. Phys. Chem. B 108 (2004) 10955.
[19] W. Tang, G. Henkelman, J. Chem. Phys. 130 (2009) 194504.
[20] J.K. Nørskov, J. Rossmeisl, A. Logadottir, L. Lindqvist, J.R. Kitchin, T. Bligaard, H. Jónsson, J. Phys. Chem. B 108 (2004) 17886.
[21] T. Bligaard, J. Nørskov, S. Dahl, J. Matthiesen, C. Christensen, J. Sehested, J. Catal. 224 (2004) 206.
[22] J.L. Fernández, D.A. Walsh, A.J. Bard, J. Am. Chem. Soc. 127 (2005) 357.
[23] V.R. Stamenkovic, B. Fowler, B.S. Mun, G. Wang, P.N. Ross, C.A. Lucas, N.M. Marković, Science 315 (2007) 493.
[24] S. Koh, P. Strasser, J. Am. Chem. Soc. 129 (2007) 12624.
[25] O. Savadogo, K. Lee, K. Oishi, S. Mitsushima, N. Kamiya, K.-I. Ota, Electrochem. Commun. 6 (2004) 105.
[26] C.-Y. Lu, G. Henkelman, J. Phys. Chem. Lett. 2 (11) (2011) 1237.
[27] W. Tang, L. Zhang, G. Henkelman, J. Phys. Chem. Lett. 2 (2011) 1328.
[28] F. Fouda-Onana, S. Bah, O. Savadogo, J. Electroanal. Chem. 636 (2009) 1.
[29] X. Wang, N. Kariuki, J.T. Vaughey, J. Goodpaster, R. Kumar, D.J. Myers, J. Electrochem. Soc. 155 (2008) B602.
[30] B. Hammer, J.K. Nørskov, Nature 376 (1995) 238.
[31] N.S. Froemming, G. Henkelman, J. Chem. Phys. 131 (23) (2009) 234103.
[32] J.X. Wang, H. Inada, L. Wu, Y. Zhu, Y. Choi, P. Liu, W.-P. Zhou, R.R. Adzic, J. Am. Chem. Soc. 131 (47) (2009) 17298.
[33] K. Gong, D. Su, R.R. Adzic, J. Am. Chem. Soc. 132 (41) (2010) 14364.
[34] S. Pande, S.K. Ghosh, S. Praharaj, S. Panigrahi, S. Basu, S. Jana, A. Pal, T. Tsukuda, T. Pal, J. Phys. Chem. C 111 (29) (2007) 10806.
[35] P.-P. Fang, S. Duan, X.-D. Lin, J.R. Anema, J.-F. Li, O. Buriez, Y. Ding, F.-R. Fan, D.-Y. Wu, B. Ren, Z.L. Wang, C. Amatore, Z.-Q. Tian, Chem. Sci. 2 (2011) 531.
[36] A.U. Nilekar, Y. Xu, J. Zhang, M. Vukmirovic, K. Sasaki, R. Adzic, M. Mavrikakis, Top. Catal. 46 (3–4) (2007) 276.
[37] F.-J. Lai, H.-L. Chou, L.S. Sarma, D.-Y. Wang, Y.-C. Lin, J.-F. Lee, B.-J. Hwang, C.-C. Chen, Nanoscale 2 (2010) 573.
[38] G. Barcaro, A. Fortunelli, M. Polak, L. Rubinovich, Nano Lett. 11 (4) (2011) 1766.
[39] J. Hernández, J. Solla-Gullón, E. Herrero, A. Aldaz, J.M. Feliu, J. Phys. Chem. B 109 (26) (2005) 12651.
[40] J. Hernández, J. Solla-Gullón, E. Herrero, A. Aldaz, J.M. Feliu, J. Phys. Chem. C 111 (38) (2007) 14078.
[41] J. Hernández, J. Solla-Gullón, E. Herrero, J.M. Feliu, A. Aldaz, J. Nanosci. Nanotechnol. 9 (4) (2009) 2256.
[42] E.V. Carino, H.Y. Kim, G. Henkelman, R.M. Crooks, J. Am. Chem. Soc. 134 (9) (2012) 4153.
[43] R. Iyyamperumal, L. Zhang, G. Henkelman, R.M. Crooks, J. Am. Chem. Soc. 135 (15) (2013) 5521.
[44] M.H. Shao, K. Sasaki, R. Adzic, J. Am. Chem. Soc. 128 (2006) 3526.
[45] K. Sasaki, H. Naohara, Y. Choi, Y. Cai, W.-F. Chen, P. Liu, R.R. Adzic, Nat. Commun. 3 (2012) 1115.
[46] L. Zhang, G. Henkelman, J. Phys. Chem. C 116 (2012) 20860.
[47] L. Zhang, G. Henkelman, ACS Catal. 5 (2) (2015) 655.
[48] L. Zhang, H.Y. Kim, G. Henkelman, J. Phys. Chem. Lett. 4 (2013) 2943.